











Transmission of 300 GBd QAM Signals Over Trans-Oceanic Distances Using Optical Arbitrary Waveform Generation and Measurement (OAWG/OAWM)

Daniel Drayss , Haik Mardoyan , Senior Member, IEEE, Dengyang Fang , Sylvain Almonacil , Member, IEEE, Alban Sherifaj, Amirhossein Ghazisaeidi , Senior Member, IEEE, Mohamed Kelany, Carina Castineiras Carrero , Thomas Zwick , Fellow, IEEE, Sebastian Randel, Senior Member, IEEE, Wolfgang Freude , Life Senior Member, IEEE, Jérémie Renaudier , Senior Member, IEEE, and Christian Koos 

(Top-Scored Paper)

Abstract—To sustain the persistent traffic growth in optical networks, symbol rates are continuously increasing, in particular in long-haul and submarine systems, where efficient exploitation of the installed fiber infrastructure is key. However, while commercial long-haul transceivers already offer symbol rates of 200 GBd, exploring the potential of transmission at symbol rates beyond this landmark still represents a challenge. One of the main difficulties is to reliably generate and analyze high-quality quadrature

amplitude modulation (QAM) signals at bandwidths of more than 200 GHz, exceeding the capabilities of available test and measurement instrumentation. In this paper, we demonstrate the potential of high-symbol-rate transmission at 300 GBd over trans-oceanic distances, exploiting the concepts of optical arbitrary waveform generation (OAWG) and optical arbitrary waveform measurement (OAWM) for synthesizing and analyzing the associated data signals. Using dual-polarization probabilistic-constellation-shaped (PCS) 36QAM signals, we achieve net bit rates of 2.45 Tbit/s over 1815 km. For PCS-16QAM signals, the transmission distance is extended to 9680 km while supporting a net bit rate of 1.63 Tbit/s. In the back-to-back setup, the net bit rate is increased to 2.88 Tbit/s using 64QAM signals. To the best of our knowledge, our experiments achieve the highest symbol rate so far transmitted over a distance exceeding 100 km. Furthermore, the demonstrated distances for target net bit rates of 1.6 Tbit/s and 2.4 Tbit/s surpass previous demonstrations by more than an order of magnitude.

Received 16 January 2025; revised 29 April 2025; accepted 7 June 2025. Date of publication 13 June 2025; date of current version 4 July 2025. This work was supported in part by EIC Transition Projects CombTools under Grant 101136978, in part by HDLN under Grant 101113260, in part by the HORIZON-ERC-2023-POC Teragear under Grant 101123567, in part by the ERC Consolidator Grant TeraSHAPE under Grant 773248, in part by the DFG Projects PACE under Grant 403188360, in part by the GOSPEL under Grant 403187440, in part by the DFG Collaborative Research Centers (CRC) WavePhenomena under Grant SFB 1173 and Grant 258734477, in part by the BMBF Project Open6GHub under Grant 16KISK010, in part by Alfried Krupp von Bohlen und Halbach Foundation, in part by the MaxPlanck School of Photonics (MPSP), and in part by the Karlsruhe School of Optics & Photonics (KSOP). (Daniel Drayss, Haik Mardoyan, Dengyang Fang, and Sylvain Almonacil contributed equally to this work.) (Corresponding authors: Daniel Drayss; Haik Mardoyan; Christian Koos.)

Daniel Drayss and Dengyang Fang are with the Institute of Photonics and Quantum Electronics (IPQ), Karlsruhe Institute of Technology (KIT), 76131 Karlsruhe, Germany, and also with the Teragear GmbH, 76227 Karlsruhe, Germany (e-mail: daniel.drayss@kit.edu).

Haik Mardoyan, Sylvain Almonacil, Amirhossein Ghazisaeidi, Carina Castineiras Carrero, and Jérémie Renaudier are with the Department of Optical Transmission, Nokia Bell Labs, 91300 Massy, France (e-mail: haik.mardoyan@nokia-bell-labs.com).

Alban Sherifaj, Mohamed Kelany, Sebastian Randel, and Wolfgang Freude are with the Institute of Photonics and Quantum Electronics (IPQ), Karlsruhe Institute of Technology (KIT), 76131 Karlsruhe, Germany.

Thomas Zwick is with the Institute of Radio Frequency Engineering and Electronics (IHE), Karlsruhe Institute of Technology (KIT), 76131 Karlsruhe, Germany.

Christian Koos is with the Institute of Photonics and Quantum Electronics (IPQ), Karlsruhe Institute of Technology (KIT), 76131 Karlsruhe, Germany, with the Institute of Microstructure Technology (IMT), Karlsruhe Institute of Technology (KIT), 76131 Karlsruhe, Germany, with Deeplight SA, 1015 Lausanne, Switzerland, with Deeplight GmbH, 76131 Karlsruhe, Germany, and also with the Teragear GmbH, Karlsruhe, Germany (e-mail: christian.koos@kit.edu).

Color versions of one or more figures in this article are available at <https://doi.org/10.1109/JLT.2025.3579802>.

Digital Object Identifier 10.1109/JLT.2025.3579802

Index Terms—Coherent communications, optical arbitrary waveform generation and measurement (OAWG/OAWM), optical fiber communication, optical frequency combs, optical multiplexing, ultra-long haul (ULH) transmission.

I. INTRODUCTION

HIGH symbol-rate optical transmission is key to support the sustained traffic growth in optical networks. Symbol rates of commercially available transceivers increased from 64 GBd in 2018 to 140 GBd in 2022 [1], [2], [3], [4] and to 200 GBd in 2024 [5], while schemes for 260 GBd and beyond are currently being investigated and corresponding ASICs are being developed using advanced CMOS nodes. Historically, the introduction of novel high-symbol-rate transmission schemes has been heralded by system-level proof-of-concept experiments that were key to demonstrating novel device technologies [6], [7], [8], [9], to testing advanced signal processing techniques [10], [11], to understanding the underlying limitations [12], and to conceiving or verifying associated mitigation techniques [13]. However, high-symbol-rate long-haul transmission demonstrations beyond the commercial state of the art have recently

become increasingly difficult. Specifically, transmission demonstrations for distances above 100 km and net bit rates above 1.6 Tbit/s per channel were so far limited to symbol rates of 192 GBd or less [14], [15], [16], [17], [18], while commercial products have already reached symbol rates of 200 GBd [5] and demonstrated a 1.6 Tbit/s transmission over a distance of 470 km [19]. One of the key challenges in maintaining the supremacy of proof-of-concept transmission experiments with respect to commercial products is the lack of test and measurement equipment that offers adequate bandwidth and signal quality at symbol rates beyond 200 GBd [6].

In this paper, we exploit the concepts of optical arbitrary waveform generation (OAWG) and optical arbitrary waveform measurement (OAWM) to demonstrate the potential of high-symbol-rate long-haul transmission at 300 GBd over transoceanic distances [20]. The signal generation at the transmitter (Tx) relies on spectrally sliced actively phase-stabilized waveform synthesis in the optical domain, which renders the bandwidth of the optical signal independent from that of the underlying digital-to-analogue converter (DAC) channels and thereby permits waveform synthesis at unprecedented bandwidth and signal quality [21], [22], [23], [24]. Similarly, detection of the 300 GBd quadrature amplitude modulation (QAM) signals at the receiver relies on spectrally sliced reception and digital signal reconstruction [25], [26], where we use an advanced scheme that can simultaneously acquire two polarizations. We explore different modulation formats and use a recirculating fiber loop that relies on erbium-doped fiber amplification only to investigate signal degradation over a large range of transmission distances. Using dual-polarization probabilistic-constellation-shaped (PCS) 36QAM signals and variable-rate forward error correction (FEC) codes, we achieve net bit rates of 2.45 Tbit/s over more than 1800 km. For slightly simpler PCS-16QAM signals, the transmission distance could be extended to 9680 km while supporting net bit rates of 1.63 Tbit/s. We further demonstrated transmission over more than 20 000 km using conventional quadrature phase-shift keying (QPSK) signaling, also at 300 GBd. To the best of our knowledge, our experiments represent the highest symbol rate so far transmitted over distance more than 100 km. Moreover, the demonstrated distances for target net bit rates of 1.6 Tbit/s and 2.4 Tbit/s exceed previous demonstrations by more than an order of magnitude, showcasing not only the outstanding performance of OAWG and OAWM for ultra-broadband optical signal generation and detection, but also the strong potential of high-symbol-rate transmission in long-haul systems.

II. CONCEPT AND EXPERIMENTAL SETUP

The concept of our demonstration and the associated experimental setup is shown in Fig. 1. The setup comprises a dual-polarization spectrally sliced OAWG transmitter [22], [23], Fig. 1(a), an amplified spontaneous emission (ASE) noise source for emulating co-propagating wavelength-division-multiplexing (WDM) channels in the C-band, a subsequent recirculating fiber loop [31], Fig. 1(b), as well as a dual-polarization spectrally sliced OAWM receiver [25], [26], Fig. 1(c). In the following, we discuss the individual subsystems in more detail.

A Dual-Polarization OAWG Transmitter

The dual-polarization 300 GBd signals are obtained by first synthesizing a single-polarization signal, exploiting a scheme similar to the one described in [22], [23], and by using a subsequent polarization division multiplexing emulator (PDME) for generating the dual-polarization signal, see Fig. 1(a). For synthesizing the single-polarization signal, we first generate an optical frequency comb (Tx comb) with phase-locked carriers. To this end, we start from a continuous-wave (CW) laser tone at an optical frequency of 193.044 THz (1552.97 nm) and modulate it via a dual-drive Mach-Zehnder modulator (MZM). The MZM is driven by a 16 GHz clock signal, which is derived directly from a 256 GSa/s AWG (Keysight M8199B) and boosted to a peak-to-peak voltage swing of 10 V by a subsequent RF drive amplifier (Driver). The drive-signal swing is much larger than the MZM's single-drive π -voltage of approximately 2.8 V, leading to a strong overmodulation and hence to a multitude of equidistant optical lines, as seen in Spectrum (A) of Fig. 1. The Tx comb is subsequently amplified by an erbium-doped fiber amplifier (EDFA), and two optical tones at frequencies $f_{Tx,1} = 192.980$ THz and $f_{Tx,2} = 193.124$ THz, spaced by $\Delta f_{Tx} = 9 \times 16$ GHz = 144 GHz, are selected by a wavelength-selective switch (WSS). The two optical tones are subsequently modulated by two independent IQ modulators (IQMs), where the corresponding IQ drive signals are designed such that two slightly overlapping spectral slices of the targeted 300 GBd signal are obtained at the IQM outputs. Spectrum (B) of Fig. 1 shows the independently measured optical spectra of the two spectral slices. Within the overlap region (OR), the targeted signal is obtained by adding the contributions of both spectral slices. As a consequence, the amplitude in each slice is reduced by a factor of two within the OR, corresponding to a 6 dB reduction of the power spectral density as seen in Spectrum (B) of Fig. 1. Using an actively phase-stabilizing signal-combining element (SCE) [23], the two spectral slices are coherently merged, thus producing the 300 GBd target waveform, see Spectrum (C) of Fig. 1. For the combined waveform at Point (C) in Fig. 1, we measure an optical signal-to-noise ratio (OSNR) of 37.1 dB with respect to the standard reference bandwidth $B_{ref} = 12.5$ GHz. Note that the combined waveform is produced by two tributary signals that have quite different OSNR levels, see Spectrum (B) of Fig. 1. More specifically, the OSNR amounts to 34.4 dB for the low-frequency slice generated by IQM 1 and to 42.3 dB for the high-frequency slice derived from IQM 2. The OSNR for IQM 2 is hence 8 dB higher than the OSNR of IQM 1. Thus, after combining both spectra, the ASE noise floor is dominated by IQM 1, and the OSNR of the combined signal is approximately 3 dB higher than that obtained for the first signal slice associated with IQM 1. Note also that all spectra are recorded after a linear polarizer to include only ASE noise that is co-polarized with the single-polarization signal of the respective slice.

To compensate for an optical phase drift $\Delta\varphi$ between the two overlapping tributary signals, the SCE relies on a control loop that consists of a 90° optical hybrid (COH28, Klyia SAS, Paris, France) as a passive combiner, a balanced photodetector (BPD) for generating an error signal U_{err} , a digital proportional-integral

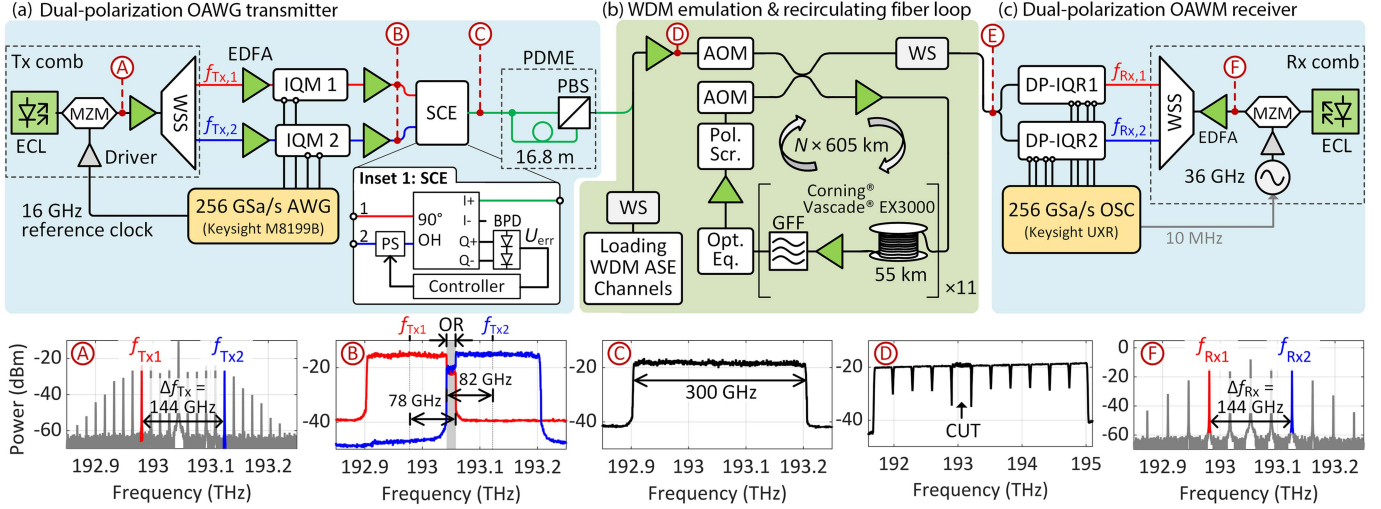


Fig. 1. Experimental setup for our 300 GBd OAWG/OAWM transmission demonstrations along with optical measurements taken at distinct points (A)–(F) within the setup. (a) A transmitter frequency comb (Tx comb) is generated by using a continuous-wave (CW) external-cavity laser (ECL) and by sending the emitted optical tone through a Mach-Zehnder modulator (MZM). The MZM is driven by a 16 GHz sinusoidal RF signal, provided by the reference clock of an arbitrary-waveform generator (AWG, Keysight M8199B, sampling rate: 256 GSa/s). Two optical tones at frequencies $f_{Tx,1} = 192.980$ THz and $f_{Tx,2} = 193.124$ THz spaced by $\Delta f_{Tx} = 9 \times 16$ GHz = 144 GHz are extracted from the MZM output by a wavelength-selective switch (WSS), see Spectrum (A). These tones serve as optical carriers for the two spectral slices and are sent to two independent IQ modulators (IQM 1 and IQM 2). The IQ drive signals are designed such that the resulting slices overlap within a 78 GHz + 82 GHz = 160 GHz-wide spectral overlap region (OR), see Spectrum (B). We measure an optical signal-to-noise ratio (OSNR) of 34.4 dB for the tributary signal generated by IQM 1 (red trace in Spectrum (B)) and of 42.2 dB for the tributary signal associated with IQM 2 (blue trace in Spectrum (B)), using the standard reference bandwidth $B_{ref} = 12.5$ GHz. The two spectral slices are subsequently combined by an actively phase-stabilizing signal-combining element (SCE) — Spectrum (C) belongs to the combined signal (OSNR = 37.1 dB), featuring a 3 dB bandwidth of 300 GHz. A polarization-division-multiplexing emulator (PDME) based on a polarization beam splitter (PBS) and a delay of 84 ns (16.8 m) is used to generate dual-polarization output waveforms. Inset 1: Implementation of the SCE. An optical hybrid (90° OH) combines the first spectral slice connected to input port “1” and the second spectral slice connected to input port “2” and produces an output signal at the “I+” port. A balanced photodetector (BPD) is used to generate an error signal U_{err} that is proportional to the phase error between the two spectrally overlapping tributaries. A digital proportional-integral (PI) controller (Controller) drives a phase shifter (PS), which acts on the second tributary signal to compensate for the phase error. A more detailed explanation and a mathematical description of the SCE concept can be found in [23]. (b) The channel under test (CUT) is combined with co-propagating wavelength-division-multiplexing (WDM) dummy channels, which are carved out of spectrally white amplified spontaneous emission (ASE) noise using a programmable WaveShaper (WS). The dummy channels are configured to emulate a WDM channel spacing of 306.25 GHz, see Spectrum (D). The combined WDM signal is injected into a recirculating fiber loop through an acousto-optic modulator (AOM). The loop consists of 11 spans of Corning® Vascade® EX3000 fiber. The fiber attenuation is compensated at the end of each span by a C-band EDFA followed by a gain-flattening filter (GFF), and the optical power across all WDM channels is additionally equalized once per 605 km loop by a dedicated optical equalizer (Opt. Eq.). A loop-synchronous polarization scrambler (Pol. Scr.) randomly varies the state of polarization. At the output of the recirculating fiber loop, a second WS (insertion loss 5 dB) selects the CUT from the WDM spectrum. (c) A two-channel dual-polarization OAWM receiver based on two dual-polarization IQ receivers (DP-IQR 1 and DP-IQR 2) and two synchronized oscilloscopes (OSC; Keysight UXR, sampling rate: 256 GSa/s) captures the CUT. The OAWM receiver relies on two tones extracted from a second frequency comb (Rx comb). The two tones are spaced by $\Delta f_{Rx} = 4 \times 36$ GHz = 144 GHz and serve as local oscillators (LOs) for coherent detection, see Spectrum (F).

(PI) controller, and a phase shifter (PS, FPS-003, General Photonics, now part of Luna Innovations) that acts on one of the tributary signals at the input port of the passive combiner, see [23] for a more detailed explanation. Note that both the optical hybrid and the phase shifter introduce additional optical losses. The attenuation measured from the upper input port of the SCE, labeled “1” in Inset 1 of Fig. 1(a), to the SCE output port, labeled “I+” amounts to 10 dB and includes both the intrinsic splitting loss of the optical hybrid as well as excess losses. For the lower input port of the SCE, labeled “2” in Inset 1 of Fig. 1(a), an attenuation of approximately 7.5 dB was measured at the “I+” output port, including 0.5 dB insertion loss of the phase shifter as well as 7 dB splitting and excess loss for the optical hybrid. These losses are compensated for by EDFAs before the SCE and after the PDME, see Fig. 1(a) and (b). Since the optical power levels are sufficiently high in this part of the setup, the OSNR degradation associated with the re-amplification is negligible. Note also that the losses of the passive combiner could be reduced by using a single-polarization optical hybrid, a 3×3

multi-mode interference (MMI) coupler [23], or a wavelength-selective combiner, such as an arrayed waveguide grating. The generation of the error signal U_{err} in the SCE relies on the interference of signal components in the 16 GHz-wide OR, see Spectrum (B) in Fig. 1. Close to the operating point $\Delta\varphi = 0$ of the control loop, the error signal U_{err} is essentially proportional to the phase error $\Delta\varphi$, such that a simple PI controller can be used for the phase stabilization, see [23] for a more detailed mathematical description. If the phase error $\Delta\varphi$ equals zero, the overlapping spectral components interfere constructively at the main output port of the SCE, yielding the target waveform. Note that the 16 GHz-wide OR, which corresponds to approximately 5.3 % of the target-signal bandwidth of 300 GHz, could be significantly reduced. In our experiments, the choice of the rather large OR was a consequence of the fact that the synchronized optical frequency comb at the transmitter (Tx comb) had to be generated by driving the associated MZM directly with the 16 GHz reference clock of the AWG, see Fig. 1(a). As a result, the comb lines that can be selected as optical carriers

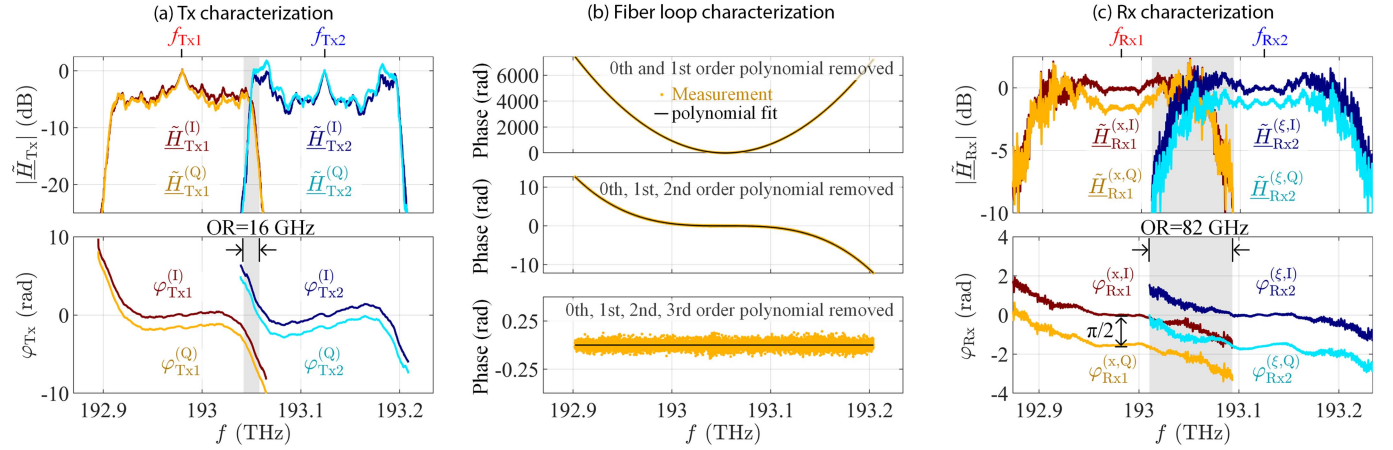


Fig. 2. Characterization and calibration of the OAWG transmitter (a), the fiber link (b), and the OAWM receiver (c). (a) The complex-valued transfer functions $\tilde{H}_{Tx1}^{(I)} = |\tilde{H}_{Tx1}^{(I)}| \exp\{j\varphi_{Tx1}^{(I)}\}$, $\tilde{H}_{Tx1}^{(Q)} = |\tilde{H}_{Tx1}^{(Q)}| \exp\{j\varphi_{Tx1}^{(Q)}\}$, $\tilde{H}_{Tx2}^{(I)} = |\tilde{H}_{Tx2}^{(I)}| \exp\{j\varphi_{Tx2}^{(I)}\}$, and $\tilde{H}_{Tx2}^{(Q)} = |\tilde{H}_{Tx2}^{(Q)}| \exp\{j\varphi_{Tx2}^{(Q)}\}$ are used to model the four transmitter channels (I_1, Q_1, I_2, Q_2). Each transfer function includes the respective arbitrary-waveform-generator (AWG, Keysight M8199B) channel (3 dB-bandwidth of 75 GHz [46]), the corresponding IQ modulator (IQM, 3 dB bandwidth of 70 GHz for IQM 1 and of 75 GHz for IQM 2), coaxial cables for connecting the AWG to the IQM, as well as all subsequent optical components up to the main output of the signal-combining element (SCE), Point © in Fig. 1(a). Note that the depicted transfer functions are shifted to the respective optical carrier frequencies, $f_{Tx,1} = 192.980$ THz and $f_{Tx,2} = 193.124$ THz, revealing a spectral overlap region (OR, gray-shaded area) that is used for active phase stabilization. The 10 dB bandwidths of the measured transfer functions are 73.3 GHz and 76.4 GHz for the first and second transmitter channel, respectively. (b) Characterization of the frequency-dependent phase shift and the dispersion associated with a single roundtrip in the recirculating fiber loop at a center frequency of 193.054 THz. Each loop roundtrip includes approximately 605 km of Corning® Vascade® EX3000 fiber, several optical amplifiers and optical filters, as well as an acousto-optic modulator (AOM) to open and to close the loop, see Fig. 1(b). To visualize higher-order contributions such as the dispersion and the dispersion slope, we fit the measured phase shift by a polynomial (coefficients p_0, p_1, p_2, p_3), Eq. (1), and subsequently subtract lower-order polynomial contributions. The top subfigure shows $\Phi_L(f) - [p_0 + p_1(f - f_0)]$, such that the combined impact of chromatic dispersion, dispersion slope, and higher-order effects remains. The middle subfigure shows $\Phi_L(f) - [p_0 + p_1(f - f_0) + p_2(f - f_0)^2]$, while the bottom subfigure depicts $\Phi_L(f) - [p_0 + p_1(f - f_0) + p_2(f - f_0)^2 + p_3(f - f_0)^3]$, representing higher-order effects only. The bottom subfigure only shows measurement noise, and we conclude that a third-order polynomial is sufficient for describing the dispersion characteristics of the loop while higher-order effects beyond p_3 can be neglected. The chromatic dispersion amounts to $C_\lambda = 12731$ ps/nm and the dispersion slope to $S_\lambda = 36.8$ ps/nm², both obtained from the polynomial fit, see Eq. (2). (c) Complex-valued transfer functions $\tilde{H}_{Rx1}^{(x,I)}$, $\tilde{H}_{Rx1}^{(x,Q)}$, $\tilde{H}_{Rx2}^{(\xi,I)}$, and $\tilde{H}_{Rx2}^{(\xi,Q)}$ associated with the response of one polarization channel (x, ξ) of each dual-polarization IQ receiver (DP-IQR) that is connected to a corresponding oscilloscope channel. The DP-IQRs rely on balanced photodetectors with a 3 dB bandwidth beyond 90 GHz (BPDV4120R, Coherent Corp., Saxonburg, Pennsylvania, USA). A second set of transfer functions is obtained for the respective other polarization (y, ψ ; not shown). The transfer functions are shifted with respect to the local oscillator (LO) frequencies, $f_{Rx,1} = 192.980$ THz and $f_{Rx,2} = 193.124$ THz. The comparatively large receiver bandwidth (10 dB-bandwidth: 113 GHz) leads to an 82 GHz-wide overlap region (OR; gray-shaded area). Note that a much smaller OR with bandwidths below 1 GHz would be sufficient for correctly stitching the spectral slices [26].

are spaced by an integer multiple of 16 GHz, and we chose a spacing of 9×16 GHz = 144 GHz for our experiments. This choice, however, enforced relatively high electrical bandwidths of 78 GHz for the first and of 82 GHz for the second transmitter channel to cover an overall bandwidth of 304 GHz which was required to accommodate the 300 Gb/s root-raised-cosine (RRC) signal with a roll-off factor of approximately 1.3% — the reason for the slightly asymmetric choice of the bandwidths of the two spectral slices is explained below. This choice directly dictates the width of the OR to 78 GHz + 82 GHz – 144 GHz = 16 GHz. Using a frequency comb that is more flexible with respect to the chosen line spacing, one could reduce the OR and increase the bandwidth of the generated signal accordingly — we have demonstrated OAWG with significantly smaller overlaps of, e.g., 1% of the target-signal bandwidth, which still achieve high constellation signal-to-noise ratios (CSNR) of up to 19 dB [23].

For best performance of the OAWG system, the characteristics of the OAWG transmitter must be compensated by appropriate digital pre-distortion techniques. To this end, we first characterize the two OAWG channels using a calibrated reference IQ receiver, following the steps described in [23]. The amplitude and phase of the resulting four complex-valued transfer

functions $\tilde{H}_{Tx,1}^{(I)}(f)$, $\tilde{H}_{Tx,1}^{(Q)}(f)$, $\tilde{H}_{Tx,2}^{(I)}(f)$, and $\tilde{H}_{Tx,2}^{(Q)}(f)$ for the in-phase and quadrature components of the two transmitter channels are shown in Fig. 2(a). Note that the depicted frequency responses include all system components up to the main output port of the SCE, i.e., they account for the transfer functions of both the respective AWG channel and the associated IQM. Note also that the second transmitter channel associated with IQM 2 has a 10 dB bandwidth of 76.4 GHz, which is slightly larger than the 73.3 GHz offered by the first transmitter channel associated with IQM 1. To account for this asymmetry, we split the target signal with a total optical bandwidth of 304 GHz in a slightly asymmetric way such that the more broadband IQM 2 covers a slice with a bandwidth of 2×82 GHz = 164 GHz, whereas the slice covered by the more narrowband IQM 1 is only 2×78 GHz = 156 GHz wide, see Spectrum (B) in Fig. 1. Accounting for the 16 GHz-wide OR, we obtain the required optical bandwidth of 304 GHz. The asymmetric splitting is accomplished by positioning the two comb tones such that their average frequency $(f_{Tx,1} + f_{Tx,2}) / 2$ is 2 GHz below the spectral center of the targeted data signal and by assigning the spectral slices accordingly. This leads to an asymmetry in the slice widths of 4 GHz — slightly larger than the 3.1 GHz

of bandwidth asymmetry of the two underlying transmitter channels. This choice was deliberately made to additionally account for an OSNR difference of the two transmitter channels — IQM 2 offered a higher OSNR than IQM 1, allowing for a stronger pre-distortion without excessively sacrificing signal quality.

After proper synthesis and feedback-stabilized coherent combination of the two signal slices, the resulting 300 GBd single-polarization waveform is sent through a polarization-division-multiplexing emulator (PDME) that is based on a split-and-delay architecture and that generates a dual-polarization output signal. The delay between both polarizations in the PDME is 84 ns. The dual-polarization signal is then fed as channel under test (CUT) to the second part of our setup, that comprises the WDM emulation setup and the recirculating fiber loop, see Fig. 1(b).

B WDM Emulation and Fiber Transmission

To emulate multi-channel WDM transmission, the CUT is combined with co-propagating dummy signals that are carved out of spectrally white amplified spontaneous emission (ASE) noise using a programmable WaveShaper (WS, WaveShaper A-Serie, Coherent Corp., Saxonburg, Pennsylvania, USA). The resulting WDM stream has a channel spacing of 306.25 GHz, see Spectrum ① of Fig. 1, and is injected into a recirculating fiber loop that is designed to emulate a multi-span submarine transmission link, Fig. 1(c). More specifically, the loop consists of 11 spans of 55 km Corning® Vascade® EX3000 fibers with a nominal loss coefficient of 0.157 dB/km, a chromatic dispersion coefficient of 20.5 ps/(nm km), a dispersion slope of 0.06 ps/(nm² km), and an effective area of 150 μm², all specified for a wavelength of 1550 nm [31]. Each loop hence corresponds to a transmission of approximately 605 km. The fiber attenuation is compensated for at the end of each 55 km span by a C-band EDFA (noise fig. 4.5 dB) followed by a gain-flattening filter (GFF), see Fig. 1(b). Note that, despite the use of a GFF in each span, the spectrum experiences a slight tilt of 2.4 dB over the entire bandwidth of 3.3 THz after propagating once through the eleven fiber spans. This tilt would increase to an unrealistically high value of approximately 80 dB for the 33 loops used for emulating the longest transmission distance of 20 000 km, see Fig. 4(b). The residual spectral tilt is therefore carefully compensated for once per loop roundtrip using an appropriately programmed WSS as a separate optical equalizer, labelled Opt. Eq. in Fig. 1(b). To confirm the effectiveness of the additional optical gain equalizer, we measure the residual gain tilt after propagating the light eight times through the fiber loop, corresponding to $8 \times 11 = 88$ spans. We find an overall residual gain tilt below 0.4 dB, corresponding to a residual gain tilt of only 0.05 dB for each of the eight loops, each comprising 11 fiber spans. The optical equalizer is followed by a loop-synchronized polarization scrambler (Pol. Scr.), see Fig. 1(b), which randomly varies the signal's state of polarization across the Poincaré sphere. The loop can be opened and closed by an acousto-optic modulator (AOM). Note that the AOM, the polarization scrambler, and the additional optical equalizer contribute additional intra-loop losses of approximately 6 dB,

0.5 dB, and 5 dB, respectively, which would not occur in real-world transmission links. These additional losses, even though they are compensated by additional amplifiers, degrade the OSNR slightly. Our experiments might hence slightly underestimate the transmission distance that could be achieved without these additional elements.

For efficient digital dispersion compensation of the received QAM signals, we measure the dispersion C'_λ and the dispersion slope S'_λ introduced by a single roundtrip in the recirculating fiber loop at a center frequency $f_c = 193.054$ THz ($\lambda_c = 1552.9$ nm), see Fig. 2(b). To this end, we generate an optical frequency comb with comb lines at frequencies f_i , $i = 1, 2, 3, \dots$ spaced by 40 MHz using the OAWG transmitter. We then individually measure the phase of the various frequency comb lines detected at the OAWM receiver for a single roundtrip $\Phi_{\text{Rx},L1}(f_i)$, and for two consecutive roundtrips $\Phi_{\text{Rx},L2}(f_i)$. By calculating the phase difference $\Phi_L(f_i) = \Phi_{\text{Rx},L2}(f_i) - \Phi_{\text{Rx},L1}(f_i)$, the impact of the transmitter and receiver is removed from the measurement, and we obtain the frequency-dependent phase shift of a single loop. We can then perform a least-squares fit of a 3rd order polynomial model function to the extracted phases $\Phi_L(f_i)$,

$$\hat{\Phi}_L(f) = p_3(f - f_c)^3 + p_2(f - f_c)^2 + p_1(f - f_c) + p_0. \quad (1)$$

Based on the fit parameters p_2 and p_3 , we determine the chromatic dispersion C_λ and dispersion slope S_λ introduced by each roundtrip in the fiber loop at the center frequency f_c ,

$$C_\lambda(f_c) = \frac{f_c^2 p_2}{\pi c_0} = 12731 \frac{\text{ps}}{\text{nm}},$$

$$S_\lambda(f_c) = -\left(\frac{3f_c^4 p_3}{\pi c_0^2} + \frac{2f_c^3 p_2}{\pi c_0^2}\right) = 36.8 \frac{\text{ps}}{\text{nm}^2}, \quad (2)$$

where $c_0 = 299792458$ m/s is the vacuum speed of light. The top panel of Fig. 2(b) shows the measured phase profile (yellow dots) along with the polynomial fit (black line). For the sake of better visibility, we have removed the phase offset p_0 and the group delay associated with p_1 , since they are not relevant for the link characteristics. To check whether the third-order polynomial approximation is sufficient, we subsequently subtract the quadratic contribution associated with p_2 and the cubic contribution associated with p_3 from the measured frequency-dependent phase and the associated polynomial fit, revealing that contributions above 3rd order can be neglected, see bottom panel of Fig. 2(b).

C Dual-Polarization OAWM Receiver

To detect the received waveform, we use two dual-polarization IQ receivers (DP-IQRs) and two phase-locked local oscillator (LO) tones at frequencies $f_{\text{Rx},1} \approx f_{\text{Tx},1}$ and $f_{\text{Rx},2} \approx f_{\text{Tx},2}$ for spectrally sliced OAWM, Fig. 1(c). The phase-locked LO tones are spaced by $\Delta f_{\text{Rx}} = 144$ GHz and extracted from a receiver frequency comb (Rx comb), see Spectrum ② of Fig. 1, that is generated by modulating a CW laser tone with an MZM driven by a 36 GHz sine wave. We calibrate the OAWM receiver by using a femtosecond laser as an optical reference waveform, see [27] and [28] for a detailed description of the calibration technique.

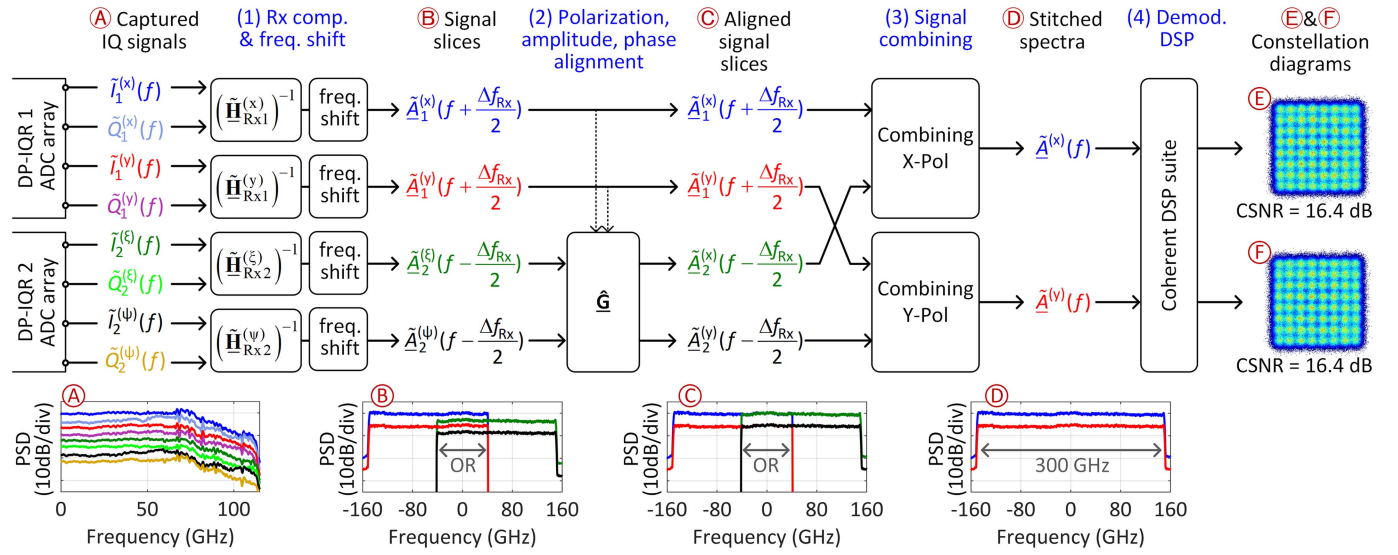


Fig. 3. Digital signal processing (DSP) steps used for reconstructing the 300 GBd dual-polarization QAM signals from the captured in-phase and quadrature components $\tilde{I}_1^{(x)}, \tilde{Q}_1^{(x)}, \tilde{I}_1^{(y)}, \tilde{Q}_1^{(y)}, \tilde{I}_2^{(\xi)}, \tilde{Q}_2^{(\xi)}, \tilde{I}_2^{(\psi)}, \tilde{Q}_2^{(\psi)}$ of the various receivers and polarizations, see Inset (A). In a first step, the frequency response of the dual-polarization IQ receiver (DP-IQR) is corrected for, Eq. (4), and a frequency shift according to the respective LO comb tone is applied, leading to overlapping spectral slices $\tilde{A}_1^{(x)}(f + \Delta f_{Rx}/2)$, $\tilde{A}_1^{(y)}(f + \Delta f_{Rx}/2)$, $\tilde{A}_2^{(\xi)}(f - \Delta f_{Rx}/2)$, and $\tilde{A}_2^{(\psi)}(f - \Delta f_{Rx}/2)$ for the x- and y-polarization at DP-IQR 1 and the ξ and ψ -polarization at DP-IQR 2, see Inset (B). The overlap regions (OR) are exploited to align amplitude, phase, and polarization of the second spectral slice to the respective first spectral slice using a linear transformation \tilde{G} , see Eqs. (5) and (6). The resulting aligned spectral slices $\tilde{A}_1^{(x)}(f + \Delta f_{Rx}/2)$, $\tilde{A}_1^{(y)}(f + \Delta f_{Rx}/2)$, $\tilde{A}_2^{(\xi)}(f - \Delta f_{Rx}/2)$, and $\tilde{A}_2^{(\psi)}(f - \Delta f_{Rx}/2)$, see Inset (C), are combined with their respective counterpart, leading to the stitched output spectra $\tilde{A}^{(x)}(f)$ and $\tilde{A}^{(y)}(f)$, see Inset (D). Finally, a standard dual-polarization coherent DSP suite consisting of chromatic dispersion compensation, complex 2×2 MIMO adaptive equalization, decimation at one sample per symbol, frequency offset and carrier phase recovery, as well as least-mean square equalization is used to demodulate the QAM signals. Insets (E) and (F) show exemplary constellation diagrams for a 300 GBd dual-polarization 64QAM signal along with the respective constellation signal-to-noise ratio (CSNR), measured in an optical back-to-back configuration. Note that the power spectral densities (PSD) in Insets (A) to (D) have a resolution bandwidth (RBW) of 1 GHz and are vertically offset for better visibility.

From the calibration measurements, we obtain four complex-valued transfer functions $\tilde{H}_{Rx1}^{(x,I)}(f)$, $\tilde{H}_{Rx1}^{(x,Q)}(f)$, $\tilde{H}_{Rx1}^{(y,I)}(f)$, and $\tilde{H}_{Rx1}^{(y,Q)}(f)$ for the I and Q component of the x- and the y-polarization of the first DP-IQR, and another four transfer functions, $\tilde{H}_{Rx2}^{(\xi,I)}(f)$, $\tilde{H}_{Rx2}^{(\xi,Q)}(f)$, $\tilde{H}_{Rx2}^{(\psi,I)}(f)$, and $\tilde{H}_{Rx2}^{(\psi,Q)}(f)$ for the two quadratures of the ξ - and the ψ -polarization of the second DP-IQR, see Fig. 2(c) for a plot of four exemplary transfer functions. Note that different subscripts (x, y) and (ξ , ψ) were chosen for the polarizations detected at the two DP-IQRs since they do not refer to the same polarization state at the input of the OAWM receiver, marked by Point (E) in Fig. 1. Specifically, the input signal is first split by a standard fiber-based power splitter, which is not polarization-maintaining, and the two partial signals are routed through separate standard single-mode fibers to the two DP-IQRs. The polarization rotation in these fibers is generally not the same, and the two distinct polarization states detected by the two DP-IQRs do hence not correspond to the polarization state at the receiver input port in Point (E). Taken together, the overall eight transfer functions $\tilde{H}_{Rx1}^{(x,I)}(f)$, $\tilde{H}_{Rx1}^{(x,Q)}(f)$, $\tilde{H}_{Rx1}^{(y,I)}(f)$, $\tilde{H}_{Rx1}^{(y,Q)}(f)$, $\tilde{H}_{Rx2}^{(\xi,I)}(f)$, $\tilde{H}_{Rx2}^{(\xi,Q)}(f)$, $\tilde{H}_{Rx2}^{(\psi,I)}(f)$, and $\tilde{H}_{Rx2}^{(\psi,Q)}(f)$ fully characterize the OAWM receiver, except for slow time-dependent phase and polarization drifts, that need to be accounted for by an appropriate dual-polarization signal reconstruction technique as

described below. All measured transfer functions show a 10 dB bandwidth of 113 GHz, which in combination with a comb line spacing of $\Delta f_{Rx} = 144$ GHz leads to an 82 GHz-wide OR, see gray-shaded area in Fig. 2(c). Note that this OR is much wider than needed — we have previously shown reliable signal reconstruction with much smaller overlap regions (< 1 GHz) [26].

For proper signal reconstruction and demodulation, we additionally account for slow phase, amplitude, and polarization drifts between individually measured spectral slices. These drifts are unavoidable in a fiber-based setup and must hence be determined and compensated individually in each measurement. The signal reconstruction, illustrated in Fig. 3, comprises four DSP steps and starts from the overall eight captured in-phase and quadrature signal components $\tilde{I}_1^{(x)}, \tilde{Q}_1^{(x)}, \tilde{I}_1^{(y)}, \tilde{Q}_1^{(y)}, \tilde{I}_2^{(\xi)}, \tilde{Q}_2^{(\xi)}, \tilde{I}_2^{(\psi)}, \tilde{Q}_2^{(\psi)}$ as recorded by the ADC-array, see Inset (A) of Fig. 3 for the corresponding power spectral densities. In the first step, the frequency response of the individual IQ detection channels is compensated based on the independently measured transfer functions $\tilde{H}_{Rx\nu}^{(q,I)}(f)$ and $\tilde{H}_{Rx\nu}^{(q,Q)}(f)$, where the subscript $\nu \in \{1, 2\}$ refers to DP-IQR 1 or DP-IQR 2, respectively, while the superscript $q \in \{x, y, \xi, \psi\}$ denotes the corresponding polarization, i.e., $q \in \{x, y\}$ for DP-IQR 1 and $q \in \{\xi, \psi\}$ for DP-IQR 2. More specifically, we construct a 2×2 transfer matrix $\tilde{H}_{Rx\nu}^{(q)}(f)$ for each DP-IQR ν

and each polarization q that relies on the corresponding transfer functions $\tilde{H}_{\text{RX}\nu}^{(q,1)}(f)$ and $\tilde{H}_{\text{RX}\nu}^{(q,Q)}(f)$ and that relates the complex-valued baseband signal spectrum $\tilde{A}_\nu^{(q)}(f)$ to the spectra $\tilde{I}_\nu^{(q)}(f)$ and $\tilde{Q}_\nu^{(q)}(f)$ measured at the in-phase and quadrature output of the corresponding DP – IQRV, see [27] for details,

$$\begin{bmatrix} \tilde{I}_\nu^{(q)}(f) \\ \tilde{Q}_\nu^{(q)}(f) \end{bmatrix} = \underbrace{\begin{bmatrix} \tilde{H}_{\text{RX}\nu}^{(q,1)}(f) & \tilde{H}_{\text{RX}\nu}^{(q,1)*}(-f) \\ \tilde{H}_{\text{RX}\nu}^{(q,Q)}(f) & \tilde{H}_{\text{RX}\nu}^{(q,Q)*}(-f) \end{bmatrix}}_{\tilde{\mathbf{H}}_{\text{RX}\nu}^{(q)}(f)} \begin{bmatrix} \tilde{A}_\nu^{(q)}(f) \\ \tilde{A}_\nu^{(q)*}(-f) \end{bmatrix}. \quad (3)$$

The baseband signal spectrum $\tilde{A}_\nu^{(q)}(f)$ is then reconstructed from the measured IQ spectra by inverting Eq. (3),

$$\begin{bmatrix} \tilde{A}_\nu^{(q)}(f) \\ \tilde{A}_\nu^{(q)*}(-f) \end{bmatrix} = \left(\tilde{\mathbf{H}}_{\text{RX}\nu}^{(q)}(f) \right)^{-1} \begin{bmatrix} \tilde{I}_\nu^{(q)}(f) \\ \tilde{Q}_\nu^{(q)}(f) \end{bmatrix}. \quad (4)$$

Note that negative- and positive-frequency components of the real-valued measured signals $\tilde{I}_\nu^{(q)}(f)$ and $\tilde{Q}_\nu^{(q)}(f)$ contain redundant information, such that only the top line of Eq. (4) needs to be evaluated, see [27] for a more detailed discussion. Subsequently, a frequency shift according to the respective LO comb tone is applied, resulting in four pairwise overlapping spectral slices, $\tilde{A}_1^{(x)}(f + \Delta f_{\text{RX}}/2)$, $\tilde{A}_1^{(y)}(f + \Delta f_{\text{RX}}/2)$, $\tilde{A}_2^{(\xi)}(f - \Delta f_{\text{RX}}/2)$, and $\tilde{A}_2^{(\psi)}(f - \Delta f_{\text{RX}}/2)$, as shown in Inset (B) of Fig. 3.

In the second step, amplitude, phase, and polarization drifts between the first and second spectral slice are compensated for by making use of signal components that fall into the spectral overlap region (OR) and that are therefore measured with both DP-IQRs, see gray-shaded area in Fig. 2(c) and OR indicated in Inset (B) of Fig. 3. Without loss of generality, we take the first spectral slice, $\tilde{A}_1^{(x)}(f + \Delta f_{\text{RX}}/2)$ and $\tilde{A}_1^{(y)}(f + \Delta f_{\text{RX}}/2)$, as a reference and transform amplitude, phase, and polarization of the second spectral slice, $\tilde{A}_2^{(\xi)}(f - \Delta f_{\text{RX}}/2)$ and $\tilde{A}_2^{(\psi)}(f - \Delta f_{\text{RX}}/2)$ using a linear transformation $\hat{\mathbf{G}}$ such that both spectral slices match within the OR. In our example, the OR is located around zero frequency in the baseband, $f_{\text{OR}} \in [\Delta f_{\text{RX}}/2 - B_{\text{RX}2}; -\Delta f_{\text{RX}}/2 + B_{\text{RX}1}] = [-41 \text{ GHz}; 41 \text{ GHz}]$, see Inset (B) of Fig. 3. To match the signal components in the OR, we determine a complex-valued 2×2 transformation matrix $\hat{\mathbf{G}}$ such that the mean squared error between the two amplitude spectra is minimized,

$$\hat{\mathbf{G}} = \arg \min_{\mathbf{G}} \left\{ \int_{f \in f_{\text{OR}}} \left| \tilde{A}_1^{(x)}(f + \frac{f_{\text{RX}}}{2}) - \tilde{A}_2^{(x)}(f - \frac{f_{\text{RX}}}{2}, \mathbf{G}) \right|^2 df + \int_{f \in f_{\text{OR}}} \left| \tilde{A}_1^{(y)}(f + \frac{f_{\text{RX}}}{2}) - \tilde{A}_2^{(y)}(f - \frac{f_{\text{RX}}}{2}, \mathbf{G}) \right|^2 df \right\}, \quad (5)$$

where

$$\begin{bmatrix} \tilde{A}_2^{(x)}(f - \frac{f_{\text{RX}}}{2}, \mathbf{G}) \\ \tilde{A}_2^{(y)}(f - \frac{f_{\text{RX}}}{2}, \mathbf{G}) \end{bmatrix} = \underbrace{\begin{bmatrix} C_{\text{LO}}^{(\xi)} & 0 \\ 0 & C_{\text{LO}}^{(\psi)} \end{bmatrix}}_{\mathbf{G}} \begin{bmatrix} \tilde{A}_2^{(\xi)}(f - \frac{f_{\text{RX}}}{2}) \\ \tilde{A}_2^{(\psi)}(f - \frac{f_{\text{RX}}}{2}) \end{bmatrix}. \quad (6)$$

In these relations, \mathbf{G} represents a linear transformation containing a 2×2 Jones matrix \mathbf{M}_J that models the difference of the polarization rotation in the fibers leading from the input of the OAWM receiver, Point (E) in Fig. 1, to the two DP-IQRs, as well as two complex-valued coefficients $C_{\text{LO}}^{(\xi)}$ and $C_{\text{LO}}^{(\psi)}$, that account for differences of phase and amplitude of the LO tones used for coherent detection of the two slices. The transformed signal slices are denoted as $\tilde{A}_2^{(x)}(f - f_{\text{RX}}/2, \mathbf{G})$ and $\tilde{A}_2^{(y)}(f - f_{\text{RX}}/2, \mathbf{G})$, respectively, see Inset (C) of Fig. 3. In the most general form, the transformation $\hat{\mathbf{G}}$ has eight degrees of freedom, i.e., two degrees for each complex-valued matrix element.

After compensating amplitude, phase, and polarization drifts, the spectral slices of each polarization are combined, yielding the output spectra $\tilde{A}^{(x)}(f)$ and $\tilde{A}^{(y)}(f)$, see Inset (D) in Fig. 3. The associated dual-polarization time-domain signals $\tilde{A}^{(x)}(t)$ and $\tilde{A}^{(y)}(t)$, i.e., the complex-valued envelopes of the 300 GBd dual-polarization optical signal, is then obtained by an inverse Fourier transformation.

Subsequently, we use a standard dual-polarization coherent DSP suite to recover the data contained in our optical QAM signals. This suite comprises chromatic dispersion compensation, complex 2×2 MIMO adaptive equalization, decimation at one sample per symbol, frequency-offset and carrier-phase recovery, and least-mean-square equalization. Insets (E) and (F) in Fig. 3 show exemplary constellation diagrams measured in the optical back-to-back configuration. Adaptive equalization is done using periodically distributed QPSK pilots with an overhead ratio R_p of 2.05% [29]. We do not apply any digital backpropagation for compensation of nonlinear effects. Using the demodulated signal, we independently measure the constellation signal-to-noise ratio (CSNR), the normalized generalized mutual information (NGMI), and the net bit rate (NBR). Note that the CSNR considers both noise and distortions and corresponds to the square of the reciprocal of the error vector magnitude (EVM) normalized to the average signal power [40], $\text{CSNR}_{\text{dB}} = 10 \log_{10}(1/\text{EVM}^2)$, see Supplement of Ref [23] for a more detailed explanation. The NBR is obtained by applying a flexible forward error correction (FEC) code based on a family of spatially coupled low-density parity-check (SC-LDPC) codes with code rates varying between 0.5 and 0.9 to achieve error-free decoding [29].

An interesting question is related to the oversampling ratio (OSR) at the transmitter and receiver side. Based on the analog signal bandwidths B_{RF} of around 113 GHz, see Inset (A) of Fig. 3, one may specify the OSR at the receiver side as the ratio between half the ADC sampling frequency, $f_s/2 = 128 \text{ GSa/s}$, and the analog signal bandwidth $B_{\text{RF}} = 113 \text{ GHz}$, leading to $\text{OSR}_{\text{ADC}} = f_s/(2B_{\text{RF}}) \approx 1.13$. Similarly, the oversampling

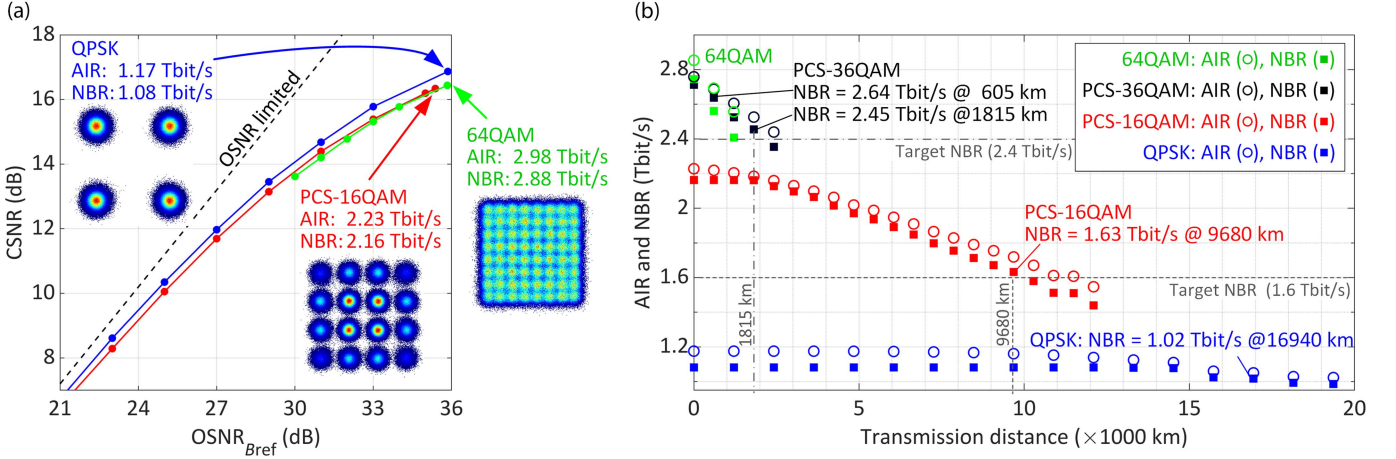


Fig. 4. Experimental results for different 300 GBd quadrature amplitude modulation (QAM) signals. (a) Constellation signal-to-noise-ratio (CSNR) as a function of the optical signal-to-noise ratio (OSNR; reference bandwidth $B_{\text{ref}} = 12.5$ GHz) measured in the optical back-to-back configuration, and exemplary constellation diagrams for a quadrature phase-shift keying (QPSK) signal, a probabilistic-constellation-shaped (PCS) 16QAM signal with an entropy of 3.8 bits/symbol/polarization, and a conventional 64QAM signal. For 64QAM, a maximum achievable information rate (AIR) of 2.98 Tbit/s and a net bit rate (NBR) of 2.88 Tbit/s is achieved. (b) AIR and NBR obtained for various transmission distances and modulation formats (QPSK, PCS-16QAM with 3.8 bits/symbol/polarization, PCS-36QAM with 4.88 bits/symbol/polarization, and 64QAM). The target net bit rates of 1.6 Tbit/s for PCS-16QAM and 2.4 Tbit/s for PCS-36QAM are achieved for transmission distances of up to 9 680 km and 1 815 km, respectively. For a transmission distance of 605 km, we measure a net bit rate of 2.64 Tbit/s using the PCS-36QAM signal with 4.88 bits/symbol/polarization.

ratio of the DAC-array at the transmitter can be calculated by considering a DAC sampling rate of 256 GSa/s along with the 78 GHz to 82 GHz analog bandwidths B_{RF} of the various IQ drive signals, see Spectrum (B) of Fig. 1. This leads to an oversampling ratio of $\text{OSR}_{\text{DAC}} \approx 1.6$ at the transmitter side.

III. TRANSMISSION EXPERIMENTS AND RESULTS

We finally use our OAWG/OAWM system for high-symbol-rate transmission over a large range of distances. In a first step, we perform optical back-to-back experiments to assess the performance of the OAWG transceiver at different optical signal-to-noise ratio (OSNR) levels. To this end, we remove the center part of the setup, that contains the WDM emulation stage and the recirculating fiber loop, Fig. 1(b), and we connect the dual-polarization OAWG transmitter via a variable optical attenuator and two cascaded EDFAs directly to the input of OAWM receiver, corresponding to Point (E) in Fig. 1(c). In this configuration, the OSNR can be varied by adjusting the attenuation setting of the variable optical attenuator, while the OSNR is measured with respect to the standard reference bandwidth $B_{\text{ref}} = 12.5$ GHz via a tap directly at the OAWM receiver input. Figure 4(a) shows the resulting constellation signal-to-noise-ratio (CSNR) of different 300 GBd QAM signals as a function of the OSNR. The CSNR saturates at high OSNR values due to imperfections of the transmitter setup and limited bandwidth of the IQ modulators. A CSNR of approx. 16.5 dB is reached for the maximum OSNR of 36 dB. Exemplary constellation diagrams for the maximum OSNR values are shown as Insets in Fig. 4(a). We also determine the achievable information rate (AIR) and the net bit rate (NBR) after FEC decoding in the optical back-to-back configuration. The AIR is calculated from the measured NGMI by considering the symbol rate $R = 300$ GBd, the pilot overhead

$R_p = 0.0205$, the signal entropy H , and the native constellation cardinality m , e.g., $m = 2$ for QPSK, $m = 4$ for PCS-16QAM, or $m = 6$ for PCS-36QAM and 64QAM, see [6], [29], [30],

$$\text{AIR} = 2R(1 - R_p)[H - (1 - \text{NGMI})m]. \quad (7)$$

To determine the net bit rate (NBR), we select the SC-LDPC code with the highest code rate r_c that allows for error-free decoding of all 841 092 symbols that were analyzed for each recording. The NBR is then calculated by replacing the NGMI in Eq. (7) by the code rate r_c [31],

$$\text{NBR} = 2R(1 - R_p)[H - (1 - r_c)m]. \quad (8)$$

In the optical-back-to-back configuration, we obtain an AIR of up to 2.98 Tbit/s and an NBR of 2.88 Tbit/s using a 64QAM constellation, Fig. 4(a).

In a second step, we perform transmission experiments over a wide range of distances, see Fig. 1 for the experimental setup. Specifically, we target an NBR of 1.6 Tbit/s using PCS-16QAM signals and an NBR of 2.4 Tbit/s using PCS-36QAM signals. To select suitable signal entropies H , we perform Monte Carlo simulations of transmission scenarios at different entropies, using an additive white Gaussian noise (AWGN) channel model. We then choose entropies of 3.8 bits / symbol / polarization for PCS-16QAM and of 4.88 bits / symbol / polarization for PCS-36QAM, which minimize the SNR requirement for the corresponding target NBR. The selected entropies should hence lead to the longest possible transmission distances for the associated target NBR. Note that we did not individually optimize the signal entropies for the various transmission distances, which could increase the demonstrated NBR and AIR further, especially for NBRs deviating from the target NBRs of 1.6 Tbit/s and 2.4 Tbit/s. In addition to the PCS-16QAM and PCS-36QAM

signals, we also transmit uniformly distributed 64 QAM and QPSK signals as a reference.

In the transmission experiments, the transmitter setup was operated at its maximum possible OSNR of 36 dB, measured at the input of the second part of the setup, containing the WDM emulation and recirculating fiber loop, see Fig. 1(b). The output power of the line EDFAs within the recirculating loop is set to 17 dBm, corresponding to the optimum launch power for a 6655 km transmission distance [31]. Figure 4(b) shows the measured AIR and NBR after FEC decoding versus transmission distance. For PCS-16QAM with an entropy of 3.8 bits/symbol/polarization, we still achieve an AIR of 1.61 Tbit/s at 11 495 km, while an NBR of 1.63 Tbit/s is obtained at 9 680 km with a code rate of $r_c = 0.74$, resulting in a net spectral efficiency of 1.63 Tbit/s / 306.25 GHz = 5.32 bit/s/Hz. Both distances exceed typical lengths of transatlantic links (approx. 7 000 km) by far. With respect to previous demonstrations [14], [15], [16], [17], [18], [19], [32], [33], [34], [35], [36], [37], [38], [39], this constitutes a ten-fold improvement in transmission distance for aggregated capacity per channel of 1.6 Tbit/s. For PCS-36QAM with an entropy of 4.88 bits/symbol/polarization, an NBR of 2.45 Tbit/s is achieved over 1 815 km with a code rate $r_c = 0.88$ and a net spectral efficiency of 8.0 bit/s/Hz. This result represents the first demonstration of long-haul single-channel 2.4 Tbit/s transmission over distances of more than 100 km. We also explored the reach of 300 GBd transmission for simple modulation formats such as QPSK, reaching distances of more than 20 000 km. This reach covers both transatlantic and transpacific distances, which are jointly referred to as ‘transoceanic’.

We also compare the back-to-back CSNR and the transmission distance achieved with our OAWG/OAWM-based scheme to the results obtained from an earlier single-slice transmission demonstration [31], which relied on essentially the same transmitter and receiver hardware (IQM1, AWG, DP-IQR1, OSC) that was used for the first spectral slice in our experiment, see Fig. 1(a). In this experiment, a 148 GBd dual-polarization PCS-16QAM signal with a target NBR of 0.8 Tbit/s was first characterized with respect to the back-to-back CSNR and then transmitted over distances of up to 7865 km [31]. To compare the single-slice CSNR results for the 148 GBd signals in [31] to those obtained for the OAWG/OAWM-based 300 GBd signals in our experiments, see Fig. 4(a), we need to consider the bandwidth difference of the two signals, i.e., we should compare the CSNR of the 148 GBd signal and of the 300 GBd signal at the same ratio of optical signal power and optical noise power within the signal bandwidth B_{sig} . This ratio is referred to as $\text{OSNR}_{B_{\text{sig}}}$ and needs to be clearly distinguished from the standard $\text{OSNR}_{B_{\text{ref}}}$ that is defined with respect to the standard reference bandwidth of $B_{\text{ref}} = 12.5$ GHz. The OSNR related to the signal bandwidth, $\text{OSNR}_{B_{\text{sig}}}$, is calculated from the $\text{OSNR}_{B_{\text{ref}}}$ by integrating the optical noise within the respective signal bandwidth B_{sig} , i.e., $\text{OSNR}_{B_{\text{sig}}} = \text{OSNR}_{B_{\text{ref}}} \times B_{\text{ref}}/B_{\text{sig}}$, where $B_{\text{sig}} = 300$ GHz for the 300 GBd signal and $B_{\text{sig}} = 148$ GHz for the 148 GBd signal. For the same $\text{OSNR}_{B_{\text{ref}}}$, the $\text{OSNR}_{B_{\text{sig}}}$ of the 300 GBd signal is hence approximately 3 dB lower than that of the 148 GBd signal. Based on this comparison we find that, for a given $\text{OSNR}_{B_{\text{sig}}}$, the CSNR of

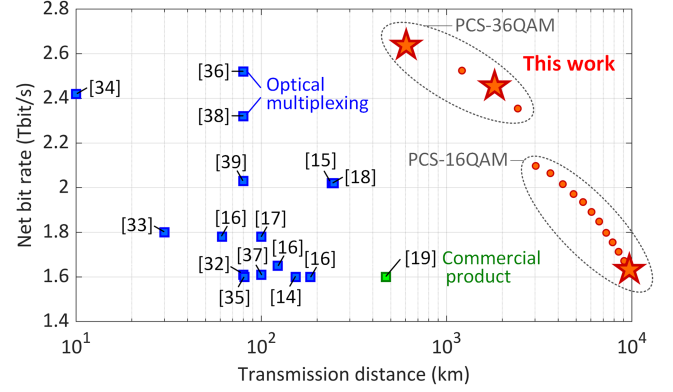


Fig. 5. Reported net bit rates (NBR) above 1.6 Tbit/s versus transmission distances ≥ 10 km [14], [15], [16], [17], [18], [19], [32], [33], [34], [35], [36], [37], [38], [39]. The results of our experiments are indicated by red markers. The stars indicate transmission distances of 605 km, 1 815 km, and 9 680 km, for which we reached net bit rates of 2.64 Tbit/s, 2.45 Tbit/s, and 1.63 Tbit/s. The combined use of OAWG and OAWM techniques can unlock an entirely new field of reference transmission experiments, bridging unprecedented distances at highest symbol rates with superior signal quality.

the OAWG-based 300 GBd signal is even slightly (0.6 dB ... 0.8 dB) higher than that of the single-slice 148 GBd signal. We attribute this to the more advanced transmitter and receiver calibration used in our OAWG/OAWM experiments, see Fig. 2 above. The improved back-to-back CSNR is consistent with the observation that the transmission distance demonstrated in our current OAWG/OAWM experiments was slightly larger than that of the previous single-slice transmission. More specifically, we achieved an NBR of 1.6 Tbit/s over 9 680 km using PCS-16QAM signals with an entropy of 3.8 bits/symbol/polarization with our OAWG/OAWM scheme, whereas the single-slice experiment reported in [31] led to an NBR of 0.8 Tbit/s over only 7865 km using also PCS-16QAM signals with an entropy of 3.8 bits/symbol/polarization. Based on this comparison, we conclude that the SCE does not introduce any relevant signal degradation.

We finally benchmark our results against recent transmission experiments for distances beyond 10 km and net per-channel bit rates beyond ≥ 1.6 Tbit/s [14], [15], [16], [17], [18], [32], [33], [34], [35], [36], [37], [38], [39] as well as against a commercial transceiver that reached 1.6 Tbit/s per channel over 470 km [19]. Figure 5 shows an overview of demonstrated net bit rates vs. transmission distance, where our results are indicated by red markers. As mentioned, the transmission distances achieved in our experiments for net bit rates of 1.6 Tbit/s and 2.4 Tbit/s exceed previous demonstrations by more than an order of magnitude. For a transmission distance of 605 km, we achieve a net bit rate of 2.64 Tbit/s, which slightly exceeds previous record demonstrations based on different optical [36], [38] or electrical [34] multiplexing techniques, even though these demonstrations did not include any co-propagating WDM channels and used much shorter fiber links. Figure 5 shows that our approach can help to unlock an entirely new field of transmission experiments, bridging unprecedented distances at highest symbol rates with superior signal quality.

IV. DISCUSSION AND APPLICATION POTENTIAL

Our transmission results discussed in Fig. 5 clearly show that OAWG- and OAWM-based systems can provide outstanding signal quality at high optical bandwidths, resulting in record-high net bit rates and unprecedented transmission distances already today. Moreover, the approaches offer outstanding bandwidth scalability, opening a direct path to signal generation and detection at symbol rates well beyond 500 GBd. For the OAWG, the bandwidth can essentially be increased by using more spectral slices, i.e., by adding more AWG channels, IQMs and associated SCEs. We have recently shown an OAWG transmitter relying on four spectral slices of approximately 80 GHz each, with which we generated high-quality 320 GBd signals [23]. Increasing the slice width to the 160 GHz used in the current experiment could already lead to symbol rates beyond 600 GBd. Similarly, the bandwidth of the OAWM receiver can be scaled further – we have already shown signal acquisition over 610 GHz using four spectral slices [27]. In one of our previous publications [28] we have conducted a detailed analysis on the bandwidth-scalability of frequency-comb-based OAWM systems, considering also the tradeoff between the number of deployed channels and the bandwidth per channel.

Another interesting aspect is the application potential of OAWG- and OAWM-based concepts in practically viable optical transceivers. This aspect requires a bit more detailed consideration. In fact, it should be noted that WDM transmission, of, e.g., two channels, each running at half the symbol rate could provide similar transmission performance as a single high-symbol-rate link in terms of the net bit rate, while reducing the technical complexity, e.g., with respect to the electrical bandwidth requirements for the underlying electronic and optoelectronic components or the effort associated with dispersion compensation. Higher symbol rates are hence not valuable per se, unless their use allows to reduce the number of components (lasers, modulators, DACs, photodetectors, ADCs, or DSP engines) that are required to cover a certain optical bandwidth and to offer a certain transmission capacity. The OAWG-based approach demonstrated here does not offer this advantage, since it relies on generating two spectrally sliced tributary signals in the first place, which are then coherently combined into a single high-symbol-rate channel. A similar argument applies to the OAWM-based receiver. This clearly limits the benefits of directly using OAWG and OAWM approaches in current optical networks.

However, there are other application fields, where OAWG and OAWM-based systems could already be of impact today. One of the lead applications could be advanced test and measurement (T&M) equipment, that overcomes the limitations of currently available AWGs and oscilloscopes and that can offer the bandwidth and signal quality required for development and testing of next-generation optical transceivers. In this respect, the key challenge of traditional T&M equipment is that it cannot adopt the most advanced CMOS technology due to economic constraints. More specifically, the development of a single 3 nm CMOS chip demands R&D investments of the order of \$40 million [45] — a cost that may be justified for high-volume applications such as optical transceivers, but that

is prohibitive for medium- and low-volume products like T&M instruments. Optoelectronic signal processing as proposed in our work can be an attractive and highly scalable solution to this problem, since the optical bandwidth can be increased in a rather straightforward way by adding more lower-bandwidth transmitter and receiver channels that can be implemented based on well-established cost-efficient CMOS nodes [28]. OAWG- and OAWM-based T&M instrumentation would hence be ideally suited for investigating high-data-rate links and for testing and benchmarking next-generation optical transceivers that may offer symbol rates of 260 GBd and beyond.

Driven by such high-end lead applications, OAWG- and OAWM-based systems might mature into fully integrated solutions that combine robustness with low cost. In a second step, such compact OAWG and OAWM systems might finally find their way into actual optical communication systems, offering a series of functional advantages such as the amenability to powerful techniques for compensating fiber nonlinearities [44] or highly flexible fully software-defined assignment of spectral resources [43] without any limitations by the underlying hardware. Moreover, OAWG concepts may play a key role for high-bandwidth photonic-electronic digital-to-analog converters (PE-DACs) that rely on phase-stabilized down-conversion of optical waveforms to the electrical domain [41]. Similarly, combining OAWM schemes with high-bandwidth modulators to translate incoming electrical signals to optical waveforms could pave a path towards photonic-electronic analog-to-digital converters (PE-ADCs) with unprecedented bandwidths [42].

V. SUMMARY

We have exploited the concepts of optical arbitrary waveform generation (OAWG) and optical arbitrary waveform measurement (OAWM) for long-haul transmission at symbol rates of 300 GBd over distances of up to 20 000 km. We demonstrated the first transatlantic transmission at a net bit rate of 1.6 Tbit/s using 300 GBd dual-polarization probabilistic-constellation-shaped (PCS) 16QAM signals. In addition, we showed a record-high net bit rate of 2.64 Tbit/s over 605 km and of 2.45 Tbit/s over 1 815 km — the latter corresponding to the longest transmission distance so far demonstrated for data rates of 2.4 Tbit/s or more. In the optical back-to-back configuration, the net bit rate could be further increased to 2.88 Tbit/s using 64QAM signals. These results prove the feasibility of next-generation long-haul coherent systems with line rates of 1.6 Tbit/s and 2.4 Tbit/s. Our experiments also show that OAWG and OAWM techniques can overcome the bandwidth limitations of currently prevailing electronic signal generation and detection schemes. OAWG and OAWM concepts may thus serve as a promising technology base for future photonic-electronic test- and measurement instruments.

CONFLICT OF INTEREST

C. Koos is a co-founder and shareholder of Deeplight SA, Lausanne, Switzerland, and Deeplight GmbH, Karlsruhe, Germany, companies engaged in commercializing chip-scale tunable lasers and frequency-comb sources. C. Koos, D. Drayss, and

D. Fang are co-founders and shareholders of Teragear GmbH, Karlsruhe, Germany, a company commercializing technologies related to photonic-electronic signal processing techniques such as optical arbitrary waveform measurement (OAWM) and optical arbitrary waveform generation (OAWG). The other authors declare no conflicts of interest.

ACKNOWLEDGMENT

The authors acknowledge Keysight Technologies for supporting this work by providing a UXR real-time scope.

REFERENCES

- [1] P. J. Winzer, D. T. Neilson, and A. R. Chraplyvy, "Fiber-optic transmission and networking: The previous 20 and the next 20 years," *Opt. Exp.*, vol. 26, no. 18, pp. 24190–24239, 2018, doi: [10.1364/OE.26.024190](#).
- [2] W. Shi, Y. Tian, and A. Gervais, "Scaling capacity of fiber-optic transmission systems via silicon photonics," *Nanophotonics*, vol. 9, no. 16, pp. 4629–4663, 2020, doi: [10.1515/nanoph-2020-0309](#).
- [3] J. Homa, "Optical networks move to metro 800G and long haul 400G," 2022. Accessed: Nov. 18, 2024. [Online]. Available: <https://www.5gtechnologyworld.com/optical-networks-move-to-metro-800g-and-long-haul-400g>
- [4] P. J. Winzer, "The future of communications is massively parallel," *J. Opt. Commun. Netw.*, vol. 15, no. 10, pp. 783–787, 2023, doi: [10.1364/JOCN.496992](#).
- [5] Ciena, "Wavelength 6," 2024. Accessed: Nov. 18, 2024. [Online]. Available: <https://www.ciena.com/products/wavelength/wavelength-6>
- [6] S. Almonacil et al., "260-GBaud single-wavelength coherent transmission over 100-km SSMF based on novel arbitrary waveform generator and thin-film niobate I/Q modulator," *J. Lightw. Technol.*, vol. 41, no. 12, pp. 3674–3679, Jun. 2023, doi: [10.1109/JLT.2023.3269740](#).
- [7] C. Doerr and L. Chen, "Silicon photonics in optical coherent systems," *Proc. IEEE*, vol. 106, no. 12, pp. 2291–2301, Dec. 2018, doi: [10.1109/JPROC.2018.2866391](#).
- [8] J. Ozaki et al., "Over-85-GHz-bandwidth InP-based coherent driver modulator capable of 1-Tb/s/λ-class operation," *J. Lightw. Technol.*, vol. 41, no. 11, pp. 3290–3296, Jun. 2023, doi: [10.1109/JLT.2023.3236962](#).
- [9] M. Xu et al., "Dual-polarization thin-film lithium niobate in-phase quadrature modulators for terabit-per-second transmission," *Optica*, vol. 9, no. 1, pp. 61–62, 2022, doi: [10.1364/OPTICA.449691](#).
- [10] J. Cho and P. J. Winzer, "Probabilistic constellation shaping for optical fiber communications," *J. Lightw. Technol.*, vol. 37, no. 6, pp. 1590–1607, Mar. 2019, doi: [10.1109/JLT.2019.2898855](#).
- [11] F. Buchali, G. Böcherer, W. Idler, L. Schmalen, P. Schulte, and F. Steiner, "Experimental demonstration of capacity increase and rate-adaptation by probabilistically shaped 64-QAM," in *Proc. Eur. Conf. Opt. Commun.*, 2015, pp. 1–3, doi: [10.1109/ECOC.2015.7341688](#).
- [12] A. D. Ellis, M. E. McCarthy, M. A. Z. A. Khateeb, M. Sorokina, and N. J. Doran, "Performance limits in optical communications due to fiber nonlinearity," *Adv. Opt. Photon.*, vol. 9, no. 3, pp. 429–503, 2017, doi: [10.1364/AOP.9.000429](#).
- [13] E. Temprana et al., "Overcoming Kerr-induced capacity limit in optical fiber transmission," *Science*, vol. 348, no. 6242, pp. 1445–1448, 2015, doi: [10.1126/science.aab1781](#).
- [14] F. Pittalà et al., "Single-carrier coherent 930G, 1.28T and 1.60T field trial," in *Proc. Eur. Conf. Opt. Commun.*, 2021, pp. 1–4, doi: [10.1109/ECOC52684.2021.9605966](#).
- [15] M. Nakamura et al., "Over 2-Tb/s net bitrate single-carrier transmission based on >130-GHz-bandwidth InP-DHBT baseband amplifier module," presented at Eur. Conf. Opt. Commun., Basel Switzerland, Sep. 18–22, 2022, Paper Th3C.1.
- [16] F. Pittalà et al., "1.71 Tb/s single-channel and 56.51 Tb/s DWDM transmission over 96.5 km field-deployed SSMF," *IEEE Photon. Technol. Lett.*, vol. 34, no. 3, pp. 157–160, Feb. 2022, doi: [10.1109/LPT.2022.3142538](#).
- [17] F. Pittalà et al., "64 Tb/s DWDM transmission over 100 km G.654D fiber using super C-band erbium-doped fiber amplification," presented at the Opt. Fiber Commun. Conf., San Diego, CA, USA, Mar. 6–10, 2022, Paper W3C.4, doi: [10.1364/OFC.2022.W3C.4](#).
- [18] M. Nakamura et al., "46.4-Tb/s full C-band 246-km transmission with net >2-Tb/s/λ WDM signals using >100-GHz-BW InP-based tx front-end," presented at Eur. Conf. Opt. Commun., Frankfurt/Main, Germany, Sep. 2024, Paper Tu4B.5.
- [19] Ciena, "Arelion achieves World's first live 1.6 Tb/s wave data transmission with Ciena's WaveLogic 6 Extreme," 2024. Accessed: Dec. 5, 2024. [Online]. Available: <https://www.ciena.com/about/newsroom/press-releases/arelion-achieves-worlds-first-live-1.6-tbs-wave-data-transmission-with-cienas-wavelogic-6-extreme>
- [20] H. Mardoyan et al., "First single-carrier transmission at net data rates of 1.6 Tb/s over 9075 km and 2.4 Tb/s over 1210 km using 300 GBd dual-polarization signals and probabilistic constellation shaping," presented at Eur. Conf. Opt. Commun., Frankfurt/Main, Germany, Sep. 22–26, 2024, Paper Th2B.
- [21] T. Henauer et al., "200 GBd 16QAM signals synthesized by an actively phase-stabilized optical arbitrary waveform generator (OAWG)," presented at Opt. Fiber Commun. Conf., San Diego, CA, USA, Mar. 06–10, 2022, Paper M21.2, doi: [10.1364/OFC.2022.M21.2](#).
- [22] D. Drayss et al., "Optical arbitrary waveform generation and measurement (OAWG/OAWM) enabling 320 GBd 32QAM transmission," presented at Conf. Lasers Electro-Opt., San Jose, CA, USA, May 07–12, 2023, Paper STh5C.8, doi: [10.1364/CLEO_SI.2023.STh5C.8](#).
- [23] D. Drayss et al., "Optical arbitrary waveform generation (OAWG) using actively phase-stabilized spectral stitching," *Light: Sci. Appl.*, 2025, to be published.
- [24] D. Fang et al., "Optical arbitrary waveform generation (OAWG) based on RF injection-locked Kerr soliton combs," in *Proc. 49th Eur. Conf. Opt. Commun.*, Hybrid Conference, Glasgow, U.K., Oct. 2023, pp. 1047–1050, doi: [10.1049/icp.2023.2431](#).
- [25] N. K. Fontaine, R. P. Scott, L. Zhou, F. M. Soares, J. P. Heritage, and S. J. B. Yoo, "Real-time full-field arbitrary optical waveform measurement," *Nature Photon.*, vol. 4, no. 4, pp. 248–254, 2010, doi: [10.1038/nphoton.2010.28](#).
- [26] D. Fang et al., "Optical arbitrary waveform measurement (OAWM) using silicon photonic slicing filters," *J. Lightw. Technol.*, vol. 40, no. 6, pp. 1705–1717, Mar. 2022, doi: [10.1109/JLT.2021.3130764](#).
- [27] D. Drayss et al., "Non-sliced optical arbitrary waveform measurement (OAWM) using soliton microcombs," *Optica*, vol. 10, no. 7, pp. 888–896, 2023, doi: [10.1364/OPTICA.484200](#).
- [28] D. Drayss, D. Fang, C. Füllner, W. Freude, S. Randel, and C. Koos, "Non-sliced optical arbitrary waveform measurement (OAWM) using a silicon photonic receiver chip," *J. Lightw. Technol.*, vol. 42, no. 14, pp. 4733–4750, Jul. 2024, doi: [10.1109/JLT.2024.337899](#).
- [29] A. Ghazisaeidi et al., "Advanced C+L-band transoceanic transmission systems based on probabilistically shaped PDM-64QAM," *J. Lightw. Technol.*, vol. 35, no. 7, pp. 1291–1299, Apr. 2017, doi: [10.1109/JLT.2017.2657329](#).
- [30] P. Zou, F. Hu, Y. Zhao, and N. Chi, "On the achievable information rate of probabilistic shaping QAM order and source entropy in visible light communication systems," *Appl. Sci.*, vol. 10, no. 12, 2020, Art. no. 4299, doi: [10.3390/app10124299](#).
- [31] S. Almonacil, H. Mardoyan, A. Ghazisaeidi, and J. Renaudier, "Transmission of 800 GBPS net bit rate per wavelength over transoceanic distance using 148-GBaud PCS-16QAM," in *Proc. Eur. Conf. Opt. Commun.*, 2023, pp. 1398–1401, doi: [10.1049/icp.2023.2569](#).
- [32] V. Bajaj, F. Buchali, M. Chagnon, S. Wahls, and V. Aref, "Single-channel 1.61 Tb/s optical coherent transmission enabled by neural network-based digital pre-distortion," in *Proc. Eur. Conf. Opt. Commun.*, 2020, pp. 1–4, doi: [10.1109/ECOC48923.2020.9333267](#).
- [33] M. Nakamura, T. Kobayashi, F. Hamaoka, and Y. Miyamoto, "High information rate of 128-GBaud 1.8-Tb/s and 64-GBaud 1.03-Tb/s signal generation and detection using frequency-domain 8×2 MIMO equalization," presented at Opt. Fiber Commun. Conf. Exhib., San Diego, CA, USA, Mar. 06–10, 2022, Paper M3H.1, doi: [10.1364/OFC.2022.M3H.1](#).
- [34] D. Che, C. Deakin, and G. Raybon, "2.4-Tb/s single-wavelength coherent transmission enabled by 114-GHz all-electronic digital-band-interleaved DACs," in *Proc. 49th Eur. Conf. Opt. Commun.*, 2023, pp. 1706–1709, doi: [10.1049/icp.2023.2672](#).
- [35] D. Che et al., "First demonstration of erbium-doped waveguide amplifier enabled multi-Tb/s ($16 \times 1.6T$) coherent transmission," in *Proc. Opt. Fiber Commun. Conf.*, 2023, Paper Th4B.3, doi: [10.1364/OFC.2023.Th4B.3](#).

- [36] H. Yamazaki et al., "Single-carrier 2.5-Tbps transmission using CSRZ-OTDM with 8×4 digital calibrator," *J. Lightw. Technol.*, vol. 42, no. 12, pp. 4317–4323, Jun. 2024, doi: [10.1109/JLT.2024.3368209](https://doi.org/10.1109/JLT.2024.3368209).
- [37] A. Kawai et al., "Single-carrier 1.6-Tb/s transmission with digital inverse multiplexing on 89-GHz bandwidth doublers," presented at the Eur. Conf. Opt. Commun., 2024, Paper Tu4B.2.
- [38] H. Yamazaki et al., "Single-carrier 224-GBaud 2.3-TBPS transmission using 30-GHz DACs and electro-optic bandwidth quadrupler," presented at the Eur. Conf. Opt. Commun., Frankfurt/Main, Germany, Sep. 2024, Paper Tu4B.4.
- [39] H. Wakita et al., "100-GHz-bandwidth InP-based on-board coherent tx front-end enabling 2-Tb/s/ λ optical transmission," presented at the Opt. Fiber Commun. Conf., San Diego, CA, USA, Mar. 24–28, 2024, Paper Th4C.2, doi: [10.1364/OFC.2024.Th4C.2](https://doi.org/10.1364/OFC.2024.Th4C.2).
- [40] R. Schmogrow et al., "Error vector magnitude as a performance measure for advanced modulation formats," *IEEE Photon. Technol. Lett.*, vol. 24, no. 1, pp. 61–63, Jan. 2012.
- [41] C. Füllner et al., "Photonic-electronic arbitrary waveform generation up to 100 GHz using active phase stabilization," *Nature Commun.*, 2025, to be published.
- [42] D. Fang et al., "320 GHz photonic-electronic analogue-to-digital converter (ADC) exploiting Kerr soliton microcombs," *Light: Sci. Appl.*, 2025, to be published.
- [43] R. Proietti et al., "Elastic optical networking by dynamic optical arbitrary waveform generation and measurement," *J. Opt. Commun. Netw.*, vol. 8, pp. 171–179, 2016.
- [44] N. K. Fontaine et al., "Fiber nonlinearity compensation by digital back-propagation of an entire 1.2-Tb/s superchannel using a full-field spectrally-sliced receiver," in *Proc. Eur. Conf. Opt. Commun.*, 2013.
- [45] D. Patel, "The dark side of the semiconductor design renaissance –fixed costs soaring due to photomask sets, verification, and validation," 2022. Accessed: Mar. 31, 2025. [Online]. Available: <https://semianalysis.com/2022/07/24/the-dark-side-of-the-semiconductor>
- [46] Keysight Technologies, "M8199B 256 GSa/s arbitrary waveform generator, data sheet," data sheet, 2023. Accessed: Apr. 28, 2025. [Online]. Available: <https://www.keysight.com/de/de/assets/3122-1928/data-sheets/M8199B-256-GSas-Arbitrary-Waveform-Generator.pdf>